Shock-Ignition Laser–Plasma Interactions in Ignition-Scale Plasmas

R. H. H. Scott,[1] K. Glize,[1] L. Antonelli,[2] M. Khan,[2] W. Theobald,[3] M. S. Wei,[3] R. Betti,[3] C. Stoeckl,[3] A. G. Seaton,[4] T. D. Arber,[5] D. Barlow,[5] T. Goffrey,[5] K. Bennett,[5] W. Garbett,[6] S. Atzeni,[7] A. Casner,[8] D. Batani,[8] C. Li,[9] and N. Woolsey[2]

[1]Central Laser Facility, STFC Rutherford Appleton Laboratory, UK
[2]York Plasma Institute, Department of Physics, University of York, UK
[3]Laboratory for Laser Energetics, University of Rochester
[4]Los Alamos National Laboratory
[5]University of Warwick, UK
[6]Atomic Weapons Establishment, UK
[7]Dipartimento SBAI, Universita` di Roma "La Sapienza," Italy
[8]CELIA, University of Bordeaux, France
[9]Massachusetts Institute of Technology

The 30-kJ OMEGA—a sub-ignition-scale laser—and a novel shallow-cone target are currently being used to study laser–plasma interactions at ablation-plasma density scale lengths and laser intensities anticipated for direct-drive shock-ignition implosions at National Ignition Facility scale. Our results show that, under these conditions, the dominant instability is convective stimulated Raman scattering (SRS) with experimental evidence of two-plasmon decay (TPD) only when the density scale length is reduced. Particle-in-cell (PIC) simulations indicate that this is due to TPD being shifted to lower densities, removing the experimental backscatter signature, and reducing the hot-electron temperature. The experimental laser–energy coupling to hot electrons was found to be 1% to 2.5%, with electron temperatures between 35 and 45 keV. Radiation-hydrodynamic simulations employing these hot-electron characteristics indicate that they should not preheat the fuel in MJ-scale shock-ignition experiments.

This work describes the first laser–plasma interaction experiment performed at ignition scale and at laser intensities of relevance to shock ignition. A novel target design was created in order to reproduce the anticipated ablation-plasma conditions for an ignition-scale laser-direct-drive implosion using a sub-ignition facility. Planar targets have an infinite radius of curvature and, therefore, the potential for long density scale lengths. Twenty of OMEGA's 60 beams can be coupled onto a planar target and arranged as cones with incidence angles of 23°, 48°, and 62°. Ten of these 20 beams (5 kJ) are used to create a long-density-scale-length ablation plasma, with the remaining ten beams (5 kJ) driving a "shock-ignition" pulse into this preformed ablation plasma. The 62° cone of beams has a high angle of incidence (θ) on target, resulting in beam reflection at low density ($n_{\text{refl}} = n_c \cos^2 \theta$, where n_{refl} is the electron density where reflection occurs), which, in turn, results in inefficient laser absorption. Simulations indicate that the absorption is as low as 60%, reducing the ablation rate and forming short density scale lengths of ~200 μm.

Laser–target coupling is improved using a novel flat-tipped, shallow-cone target and repointing the low-intensity laser beams beyond the cone axis of symmetry. The conical target has the effect of reducing the beams' effective angle of incidence, θ, significantly improving the predicted absorption to 90%. A schematic of the target and example beam position is shown in Fig. 1(a). Furthermore, the conical geometry acts to reduce the divergence of the ablation-plasma flow, further increasing the density scale length. Moreover, maintaining an open-cone geometry avoids on-axis plasma flow convergence and jet formation. Simulations used the 2-D, cylindrically symmetric Lagrangian radiation-hydrodynamic code *H2D*, with 3-D laser ray tracing, *SESAME* equations of state, multigroup diffusive radiation transport, and flux-limited thermal conductivity. The calculated density scale

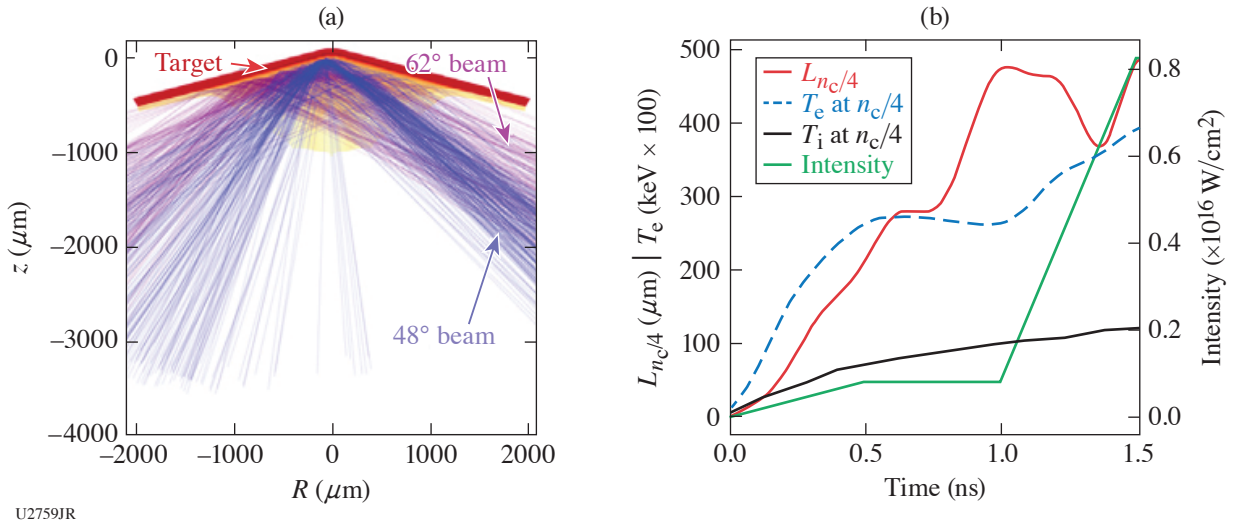

Figure 1
(a) The open-cone target design employed to generate large ablation-plasma scale lengths, shown just before the high-intensity beams switch on at 1 ns. Only two low-intensity beams are shown for clarity. (b) Simulated density scale length, electron temperature, and intensity at $n_c/4$ as a function of time using the open-cone target.

length $L_{n_c/4}$ and electron temperature T_e at the quarter-critical surface, shown in Fig. 1(b), predict ignition-scale density scale lengths of 450 μm and T_e = 3 keV at 1 ns (the time at which the high-intensity interaction commences).

The target (Fig. 1) is comprised of a 3.6-mm-diam cone with 152° opening angle and a 100-μm-diam flat tip. The laser was incident on a 40-μm-thick CH plastic ablator, backed with a 5-μm Cu diagnostic layer, followed by 30 μm of CH to tamp target expansion and prevent electron refluxing. By varying the power in the high-intensity beams on a given shot, a range of peak intensities, corrected for inverse bremsstrahlung absorption, from 8×10^{14} to 8.3×10^{15} W/cm^2 was incident on the $n_c/4$ surface, which simulations indicate was located ~200 μm from the target's front surface. The nominal delay between low- and high-intensity beams was 1 ns. A total of 12 target shots were performed.

Laser light backscattered into two of the high-intensity beams on the 23° beam cone was temporally and spectrally resolved using the full-aperture backscatter (FABS) diagnostic. Backscattered light not entering the beam port was imaged using the near backscatter imager and filtered to distinguish stimulated Brillouin scattering (~351 nm) and SRS and/or TPD (400 to 700 nm) components. Hot-electron production was diagnosed from Cu K-shell line emission using an absolutely calibrated zinc von Hamos (ZVH) spectrometer across the spectral region of 8 to 9 keV and a spherically bent quartz crystal imager (SCI) aligned to the Cu K_α spectral line at 8047.8 eV. The SCI has a narrow spectral window of 8047 to 8054 eV and records data onto an image plate (IP). The hot-electron temperature was inferred from bremsstrahlung emission using a nine-channel, differentially filtered, IP-based, time-integrated hard x-ray image plate (HXIP) over the range of 10 to 200 keV.

Figure 2(a) is an example of the backscattered light spectra with an ~450-μm density scale length. The early-time (<1-ns) backscatter signal is attributed to TPD: the narrowband spectral features above and below 702 nm have previously been shown to be indicative of TPD. As the high-intensity beams ramp up after 1 ns, a broad, bright spectral feature is seen across the 475- to 600-nm range. This broad feature is consistent with backscattered light caused by convective SRS: the backscattered light originates from densities in the range of 0.04 to 0.16 n_c—well below the ~0.22 to 0.25 n_c range where TPD is able to occur.[1] The dashed white line indicates the normalized SRS threshold (I_{thSRS}) assuming a linear density profile. This was found to consistently predict the onset of convective SRS. SRS reflectivity measured in one high-intensity beam port (B25) as a function of single-beam intensity is shown in Fig. 3(b). During the high-intensity part of the drive, no clear evidence of TPD nor absolute SRS was observed. The sharp cutoff in the signal below ~480 nm is not unexpected because the lower densities reduce convective SRS gain and enhance Landau damping; however, it may also be a signature of SRS rescatter.

Bremsstrahlung radiation emission produced via collisions of hot electrons within the target make it possible to estimate the hot-electron temperature. Measurements from the time-integrated HXIP instrument are interpreted using a Geant4-derived instrument response function[2] and χ^2 minimization techniques. Any low-energy x rays from the ablation plasma and/or Cu K-shell emission were removed by excluding the two lower-energy HXIP channels. The inferred hot-electron temperatures are in the range ~35 to 45 keV, as shown by the red ×'s in Fig. 3(a).

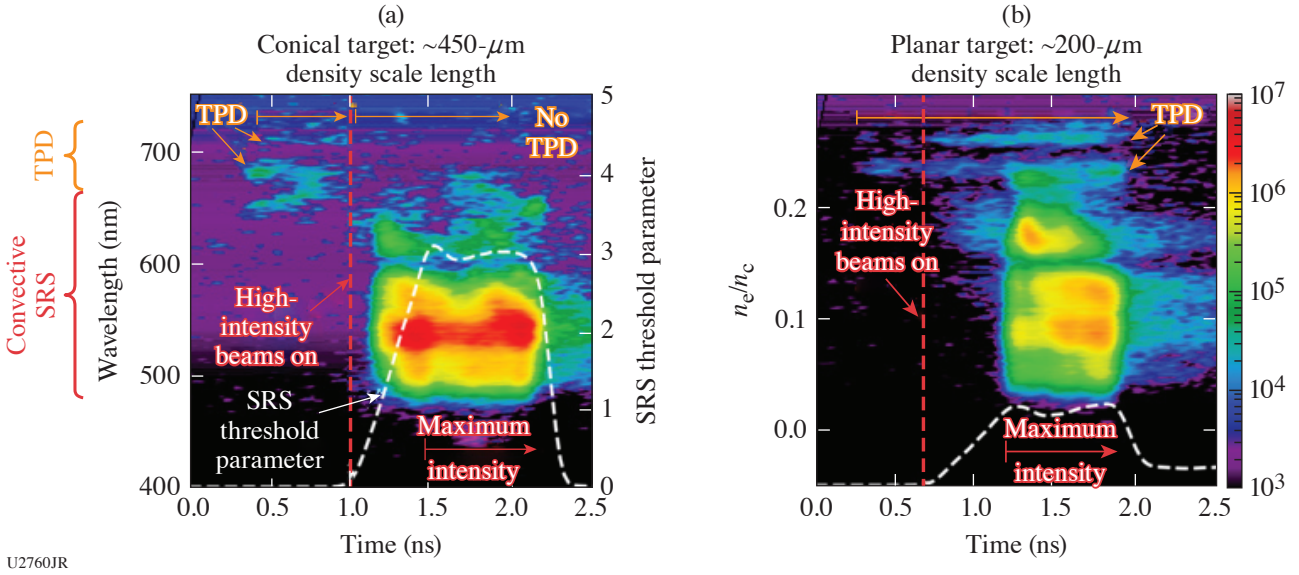

Figure 2

FABS streaked backscatter spectra: (a) Typical long-density-scale-length data: TPD is visible at early time, while during the high-intensity pulse convective SRS dominates. (b) Reduced density scale length with a planar target: TPD is visible throughout. In both cases, the low-intensity beams ramp up from 0 to 0.5 ns, while the maximum intensity is 8.5×10^{15} W/cm^2. The y axes and color scale apply to both plots with densities assuming a temperature of 3 keV. Dashed white lines indicate the SRS threshold parameter (>1 is above threshold), dashed red lines indicate the point at which the high-intensity beams turn on. In the small density scale-length case (where SRS is just above threshold), TPD is visible throughout. This is not the case in the long scale length when SRS is well above threshold. The FABS data were highly reproducible.

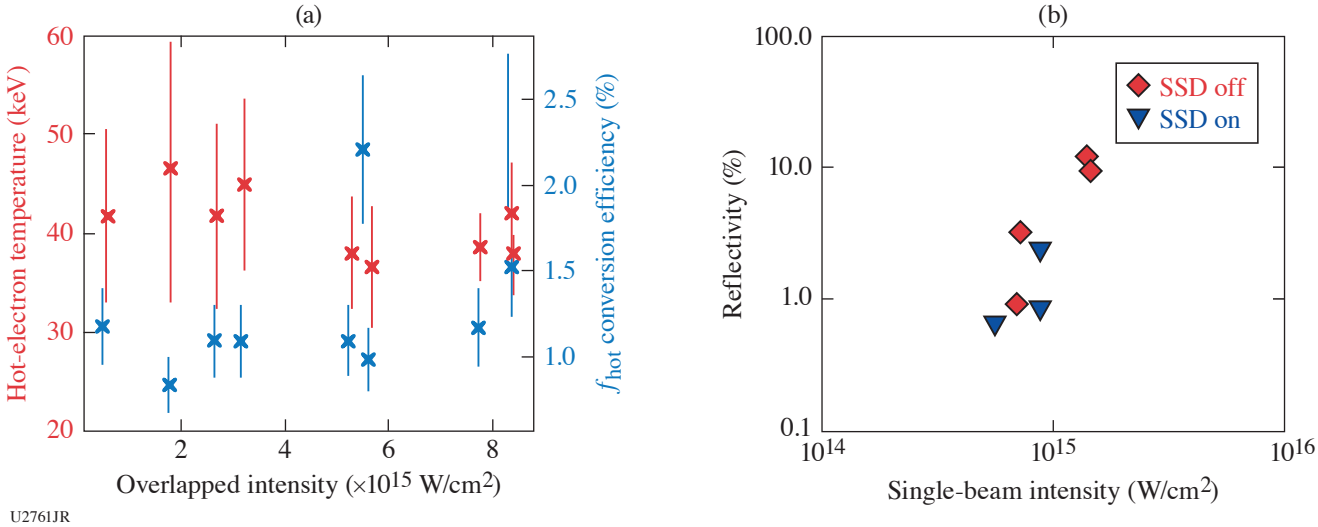

Figure 3

(a) Hot-electron temperature and total laser energy conversion to hot electrons as a function of intensity. (b) SRS reflectivity from (high-intensity) Beam 25.

The fraction of total laser energy converted to hot electrons was inferred from the K_α yield, as measured using the ZVH diagnostic. The number of K_α photons was extracted from background-subtracted ZVH data and then converted into hot-electron energy using Geant4 Monte Carlo simulations that use the cold target geometry and a 40-keV Maxwellian hot-electron population. A conversion efficiency between 1% and 2.5% [blue ×'s in Fig. 3(a)] is inferred, with some suggestion of an intensity dependence. Modeling indicates that laser-ablation–induced x-ray emission did not contribute to the signal. These data are consistent with SCI K_α images.

A comparison measurement at shorter density scale lengths is possible by reducing the delay of the high-intensity beams with respect to the low-intensity beams to 0.7 ns. This limits the plasma expansion duration, reducing the quarter-critical density scale length to ~300 μm [see Fig. 1(b)]. An alternative to laser retiming is to switch to a planar target, which further reduces the density scale length to ~200 μm. Radiation-hydrodynamic simulations predict a reduction in the electron temperature to 2.5 and 2 keV, respectively, for these two cases. At the shortest density scale length [see Fig. 2(b)], TPD is visible throughout the interaction during the low- and high-intensity parts of the laser pulse. Moreover, SRS is just above threshold during the high-intensity interaction. This contrasts with the long-scale-length case, where TPD is not observed and the high-intensity interaction significantly exceeds the SRS threshold. This suggests a transition from a small-scale-length, TPD-dominated regime to a long-scale-length regime, which appears to be dominated by convective SRS.

To investigate the relative roles of TPD and convective SRS in these experiments, 2-D plane-wave PIC simulations were performed with the code *EPOCH*[3] in a density scale length, electron (ion) temperature, and intensity regime of direct relevance to this experiment: 0.1 to 0.26 n_c, 600 μm, 4.5 (2.25) keV, and 2×10^{15} W/cm^2, respectively. These simulations show qualitative agreement with the experiments. Detailed examination of the simulations reveals that the electron plasma waves (EPW's) in the region from 0.20 to 0.24 n_c are principally caused by TPD, which explains the lack of reflected light emitted from this region and provides a compelling explanation for the "Raman gap." The occurrence of TPD at these densities is attributed to convective TPD. The low (32-keV) hot-electron temperature in the simulations—in approximate agreement with experiments—is ascribed to the fact that EPW phase velocities increase rapidly as n_e approaches $n_c/4$. As the EPW wave spectrum, which is comprised of TPD EPW's and low-density SRS EPW's, is shifted below $n_c/4$, EPW phase velocities are limited; consequently, the hot-electron temperature is reduced. At the simulated intensity, convective SRS is just above threshold; therefore, at higher intensities it would be expected that pump depletion, due to convective SRS at lower densities, would play an increasing role in governing the competition between TPD and SRS.[4] Nevertheless, we have shown that a significant factor in the dynamics observed experimentally and via simulation is likely explained by the shifting of TPD to lower densities. This shift removes the experimental $\omega_0 = 2$ "doublet" diagnostic feature, prevents convective SRS backscatter from ~0.20 to 0.24 n_c, and reduces the hot-electron temperature.

To assess the impact that the hot electrons observed in these experiments have on an implosion, we performed 2-D arbitrary Lagrangian–Eulerian radiation-hydrodynamic simulations of a 500-kJ shock-ignition implosion using the code *ODIN*. During the laser ray trace, energy is extracted from the laser (2.5%) and hot electrons are launched from the $n_c/4$ surface with a 40-keV temperature in a 45° cone. A Monte Carlo approach (benchmarked against MCNP) was used for hot-electron transport, scattering, and energy deposition. Using these experimentally measured hot-electron characteristics, the generated pressure is unaffected by the hot electrons with very little degradation in the density profile—an encouraging result for future MJ-scale shock-ignition experiments.

In summary, using a novel target design fielded on the 30-kJ OMEGA Laser System, we have found that for ablation-plasma conditions of relevance to shock ignition, the hot-electron temperature remains relatively low at 35 to 45 keV, with up to ~2.5% of the laser energy converted to hot electrons. Hydrodynamic simulations indicate the low observed hot-electron number and temperature are compatible with shock ignition at MJ scales.

This work was funded by EPSRC Grant Nos. EP/P023460/1, EP/P026486/1, and EP/P026486/1. This work has been carried out within the framework of the EUROfusion Consortium and has received funding from the EuroFUSION research and training programme under Grant Agreement Number 633053. The views and opinions expressed herein do not necessarily reflect those of the European Commission. The involved teams have operated within the framework of the Enabling Research Project: ENR-IFE19.CEA-01 Study of Direct Drive and Shock Ignition for IFE: Theory, Simulations, Experiments, Diagnostics Development.

1. W. Seka *et al.*, Phys. Plasmas **16**, 052701 (2009).
2. M. Stoeckl and A. A. Solodov, Nucl. Instrum. Methods Phys. Res. A **931**, 162 (2019).
3. T. D. Arber *et al.*, Plasma Phys. Controlled Fusion **57**, 113001 (2015).
4. C. Z. Xiao *et al.*, Nucl. Fusion **60**, 016022 (2019).